ADVANCED ENGINEERING MATERIALS
www.aem-journal.com

Local Strain Distribution in ZnO Microstructures Visualized with Scanning Nano X-Ray Diffraction and Impact on Electrical Properties

*Philipp Jordt, Stjepan B. Hrkac, Jorit Gröttrup, Anton Davydok, Christina Krywka, Niklas Wolff, Lorenz Kienle, Rainer Adelung, Olaf M. Magnussen, and Bridget M. Murphy**

The fast and contact-free detection of biomagnetic vital signs can benefit clinical diagnostics in medical care, emergency services, and scientific studies, hugely. A highly sensitive magnetoelectric sensor for the detection of biomagnetic signals combined with the piezotronic effect is a promising path to increase the signal detection limit. Herein, the results of three ZnO microrods examined by nano X-ray diffraction and current–voltage curves to investigate the crystalline structure influence on the Schottky contact properties are presented. The measurements reveal different strain distributions for the three rods and that these are linked with the electrical properties, showing that the crystalline quality has a direct influence on the Schottky contact properties. An analytical model is created to determine the influence of the stress. Although rotation of the strain orientation changes the strain appearance in the measurement, it does not affect the Schottky contact properties.

1. Introduction

Semiconductor-based magnetoelectric sensors can establish a new generation of sensor devices by combining magnetostrictive with piezoelectric materials.[1,2] These may be used to detect biomagnetic fields from the human physiology if sufficient sensitivity is met.[3–5] The magnetostrictive component reacts to an external magnetic field with a strain that is transferred into the piezoelectric component where it induces a piezoelectric potential.[1] This measurable potential change is directly correlated to the magnetic field strength. Although direct detection of the piezoelectric potential only shows limited success for biomagnetic fields, a combination of this potential with a Schottky contact at a semiconductor metal interface[6,7] provides a promising alternative, called the piezotronic effect.[8,9] The Schottky barrier height is modified by the piezoelectric potential and is detectable as an altered current flow over the contact.[10] A wide range of piezotronic applications are under development, including transistors, energy harvesting, and sensors.[11–15] The piezotronic effect was described for the first time by Wang and Song.[16] Single ZnO nanowires were deflected by a conductive atomic force microscope tip. The rod bending leads to a piezoelectric effect-induced potential which in turn changed the Schottky barrier height and thus generated a current. An in situ transmission electron microscopy (TEM) study on ZnO nanowires visualized the crystal structure and simultaneously measured the current/voltage (*IV*) curves, showing a striking impact of bending on the conductivity.[17] This was attributed to a bending-induced carrier trapping effect and reduction of the conduction channel size.

The Schottky contact and its barrier height are of great importance for the piezotronic effect,[18] for ZnO it was found that Al-containing contacts lead to an ohmic behavior, whereas Au and Ag typically result in a Schottky contact with barrier heights of ≈0.7 and ≈0.8 eV, respectively.[18] Due to vacancies at the surface, the contact formation and barrier height are hugely influenced by Fermi-level pinning,[19] which pin the ZnO Fermi level close to the oxygen defect level around 0.7 eV below the conduction band.[20] In addition, the amount of vacancies near the

P. Jordt, Dr. S. B. Hrkac, Prof. O. M. Magnussen, Dr. B. M. Murphy
Institute of Experimental and Applied Physics
Kiel University
Leibnizstr. 19, 24118 Kiel, Germany
E-mail: murphy@physik.uni-kiel.de

Dr. C. Krywka, Dr. B. M. Murphy
Ruprecht-Haensel Laboratory
Kiel University
24118 Kiel, Germany

Dr. J. Gröttrup, Dr. N. Wolff, Prof. L. Kienle, Prof. R. Adelung
Institute of Material Sciences
Kiel University
Kaiserstr. 2, 24143 Kiel, Germany

Dr. A. Davydok, Dr. C. Krywka
Helmholtz-Zentrum Hereon
Institute of Materials Physics
Geesthacht 21502, Germany

The ORCID identification number(s) for the author(s) of this article can be found under https://doi.org/10.1002/adem.202100201.

© 2021 The Authors. Advanced Engineering Materials published by Wiley-VCH GmbH. This is an open access article under the terms of the Creative Commons Attribution-NonCommercial License, which permits use, distribution and reproduction in any medium, provided the original work is properly cited and is not used for commercial purposes.

DOI: 10.1002/adem.202100201

15272648, 2021, 11, Downloaded from https://advanced.onlinelibrary.wiley.com/doi/10.1002/adem.202100201 by Christian-Albrechts-Universitat Zu Kiel, Wiley Online Library on [17/02/2026]. See the Terms and Conditions (https://onlinelibrary.wiley.com/terms-and-conditions) on Wiley Online Library for rules of use; OA articles are governed by the applicable Creative Commons License

interface strongly impacts the Au/ZnO Schottky barrier height, ranging from an ohmic behavior for a high defect rate to a Schottky contact with a barrier height of 0.48 eV at a low defect concentration, with the reverse current being decreased by 2 orders of magnitude.[21]

Cathodoluminescence spectroscopy was used to investigate the density of point defects inside ZnO wires. It was shown that the defect density and, therefore, the contact properties can be manipulated by the rod diameter and specific treatments such as ion milling and electron beam heating were used.[22]

Nano X-ray diffraction (nXRD) is an established technique to investigate the strain distribution with a high spatial resolution in microstructures.[23–25] In such a study, a 15 µm nanocrystalline CrN film was investigated utilizing a 100 nm sized X-ray beam. Inside the sample, the regions of small crystallites rich in defects were found and attributed to nucleation zones. Improved mechanical properties of thin polycrystalline multilayer films were assigned to structural defects in the multiple nucleation zones.[26] A further study utilizing nano focused diffraction investigated defect-rich GaN structures and showed that by tailoring the growth parameter an annihilation of threading dislocation is achieved.[27]

Previous nXRD studies by the authors investigated the strain behavior of micrometer-sized ZnO rods coated with magnetostrictive FeCoSiB. A rod, up to 27 µm in diameter, exhibits an intrinsic compressive strain of 5.5×10^{-4} and an additional, magnetic field induced strain of 1×10^{-4} near the ZnO interface.[28] In a further publication, it was shown that the intrinsic strain in ZnO rods can be tuned by modifying the rod dimension. The interface strain increases from 0.7×10^{-4} to 4×10^{-4} for a decreasing diameter from 50 to 5 µm.[29]

In this article, scanning nXRD and electrical examinations by *IV* measurements are combined to investigate the crystalline structure and, by doing so, link the strain distribution inside ZnO rods with the Schottky barrier's electrical properties. Utilizing the nXRD technique, the strain was measured with a high reciprocal space resolution of 10^{-5} and a spatial resolution of 200–250 nm. Compared to other semiconductors with wurtzite-type structure, e.g., AlN and GaN, ZnO microstructures provide a large piezoelectric coefficient d_{33} (5.1, 3.1, and 12.3 pm V^{-1}, respectively)[30,31] and are an ideal choice for the study of structure–property relations at the Schottky contact with X-ray sources. Three ZnO rods (R1 to R3) were investigated in this article, see the Experimental Section later for details regarding the samples and techniques. The recorded *IV* curves for the three rods vary from near ideal, rectifying behavior to nonideal behavior with huge reverse currents. The respective Bragg reflections, measured across the rod by scanning nXRD, vary from a single sharp Bragg peak for R1, to a broader peak distribution for R2 and a number of individual peaks close together for R3, as shown in Figure 2g–i. The multiple peaks are evidence of different crystal domains and their boundaries will be associated with higher defect densities in the crystal. These crystal defects result in nonideal Schottky barrier properties. Furthermore, an analytical model was created demonstrating that, depending on the measurement orientation, similar strain distributions may lead to different appearing measurements. Due to limited time available at modern synchrotron sources, required for this demanding experiment, a small selection of samples was measured. This study aims to show that the variety in the crystalline structure has considerable impact on the electrical properties, and especially the Schottky contact.

2. Results and Discussion

A sketch of the experimental geometry in **Figure 1**a shows an Au-coated ZnO microrod probed by an X-ray beam. The momentum wave vectors $\boldsymbol{k}_{in}$ and $\boldsymbol{k}_{out}$ represent, respectively, the incoming and scattered X-ray beam, given by the scattering vector $\boldsymbol{q}$ of the {000l} Bragg reflection. The scattering vector is pointing along the *c* axis of the ZnO rod and the length is inversely proportional to ZnO's lattice parameter *c*. As it is difficult to identify an unstrained region within all three samples, we chose a reference value for a nominally unstrained sample of $c \approx 5.206$ Å,

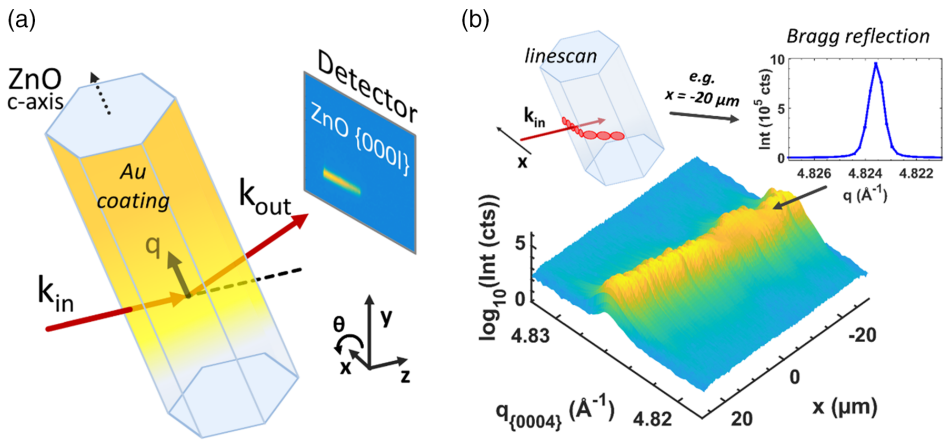

Figure 1. a) Sketch of the scattering geometry in this experiment. The incident $\boldsymbol{k}_{in}$ and scattered $\boldsymbol{k}_{out}$ wave vectors define the scattering vector $\boldsymbol{q}$, which is oriented parallel to the ZnO rod's *c* axis and probes the {000l} Bragg reflections in the Au-coated rod. The strain is sampled with a sub-µm step-sized line scan along the *x* direction. b) Example of a Bragg reflection map visualizing the Bragg reflections (inset right) intensity and *q* values as a function of the spatial position *x* of the line scan across the sample (inset left). Compared to Figure 2g–i, the strain map is tilted for an easier visualization of the concept.

© 2021 The Authors. Advanced Engineering Materials published by Wiley-VCH GmbH

which is the average value of a selection of references for ZnO at room temperature and ambient pressure.[32–35] The relative (macro)strain defined as $\varepsilon = \frac{q_0}{q} - 1$ is determined from the measured Bragg reflections position q and the value q_0 calculated from the reference lattice parameter c.[36] Macrostrain denotes an overall movement of the diffraction peak due to lattice parameter change.[37] Microstrain describes a local strain and its distribution in a coherent scattering region of the crystal leads to a broadening of the diffraction peak.[37] A positive strain is defined as tensile, describing increased lattice parameters in contrast to a negative, compressive strain referring to a shrinking of the lattice parameter. To investigate a cross section of the sample, a line scan was performed and the recorded Bragg reflection position holds access to the average, local strain with a spatial resolution of 250 nm, defined by the beam size and step size. For a line scan, the rod is moved in steps through the nano X-ray beam, as shown in the top left of Figure 1b, and a Bragg reflection (Figure 1b, top right) is recorded at each position. The Bragg reflection and its corresponding line scan spatial position x are combined in a Bragg reflection map, as exemplary shown for rod R1 in Figure 1b (further views of the map are included in Figure S1, Supporting Information).

2.1. Current-Voltage Investigations

IV curves were measured to characterize the electrical properties of the three ZnO rods, see **Figure 2**a–c. The Schottky barrier height Φ_{bh} and ideality factor n were determined for all three samples by fitting the semi logarithmic *IV* curves with a linear function. An overview of the values is shown in **Table 1** and are in agreement with previous results for ZnO Schottky contacts.[18] R1 and R2 (Figure 2a,b) show, qualitatively, the expected behavior of a rectifying Schottky contact with a distinct forward (positive voltage regime) and reverse direction.[38] But, the ideality factor for R1, in contrast to R2, is bigger and a higher reverse current is measured. It appears that the Schottky contact of R2 is of higher quality. Figure 2c shows the measured *IV* curve for R3 and, in contrast to the two previous rods, has a nonrectifying behavior with a huge reverse current and exhibits a high ideality factor. The overall behavior appears ohmic-like, even though the resistance of ≈1 MΩ is too high for an ohmic contact. It appears that a Schottky contact is present, but with a huge reverse current. The increased ideality factor and huge reverse current in both R1 and R3 are possibly caused by a generation–recombination process in the Schottky depletion region of the

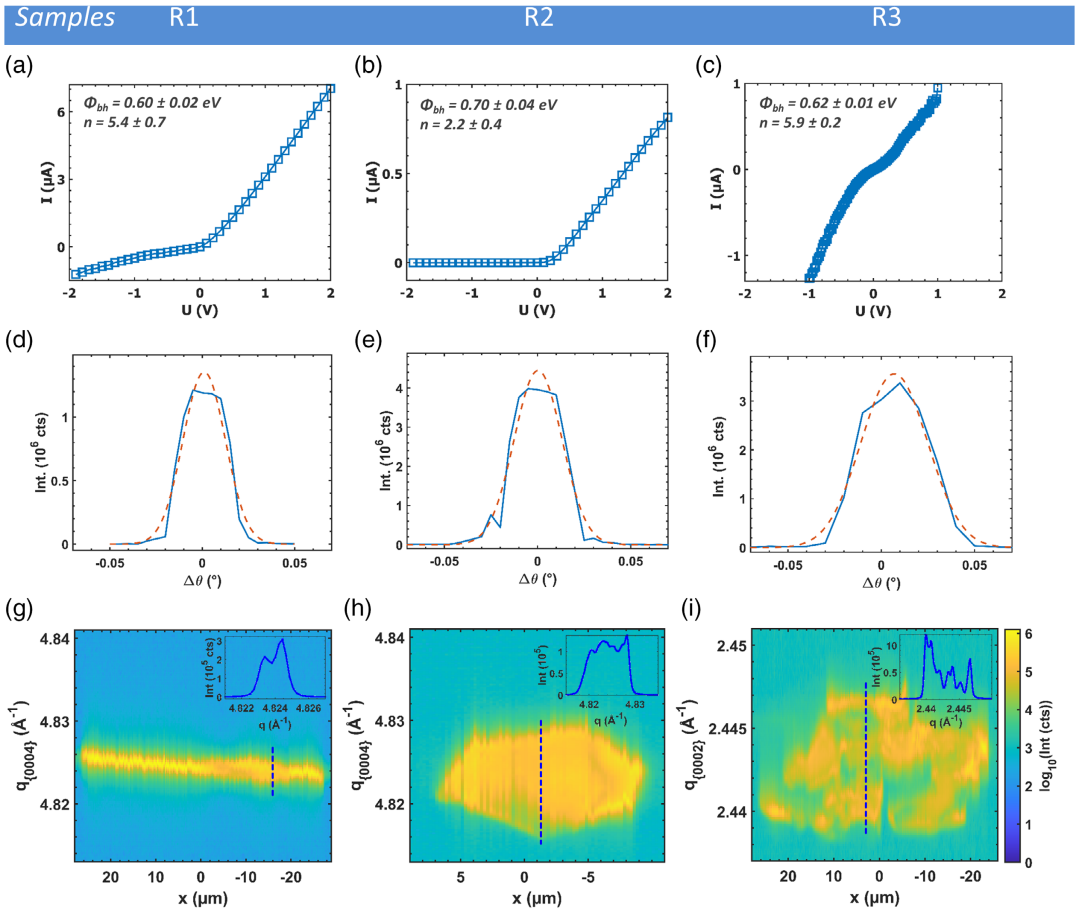

Figure 2. a–c) *IV* curves for samples R1, R2, and R3, respectively. Including the Schottky barrier height Φ_{bh} and ideality factor n of the forward current. d–f) Rocking scans collected for the three rods and fitted with a Gaussian function. Note that R1 (d) and R2 (e) are collected at Bragg reflection {0004} and R3 (f) at {0002}. g–i) Respective Bragg reflection maps for R1, R2, and R3 visualizing change across the three rods. The insets show cuts through the Bragg reflection maps at $x = -16$, -1.25, and 3 μm, respectively.

© 2021 The Authors. Advanced Engineering Materials published by Wiley-VCH GmbH

15272648, 2021, 11, Downloaded from https://advanced.onlinelibrary.wiley.com/doi/10.1002/adem.202100201 by Christian-Albrechts-Universitat Zu Kiel, Wiley Online Library on [17/02/2026]. See the Terms and Conditions (https://onlinelibrary.wiley.com/terms-and-conditions) on Wiley Online Library for rules of use; OA articles are governed by the applicable Creative Commons License

15272648, 2021, 11, Downloaded from https://advanced.onlinelibrary.wiley.com/doi/10.1002/adem.202100201 by Christian-Albrechts-Universitat Zu Kiel, Wiley Online Library on [17/02/2026]. See the Terms and Conditions (https://onlinelibrary.wiley.com/terms-and-conditions) on Wiley Online Library for rules of use; OA articles are governed by the applicable Creative Commons License

Table 1. The Schottky contact metal, the barrier height Φ_{bh}, and ideality factor n, both calculated from the *IV* curves, for the Schottky contacts of the samples R1, R2, and R3. For all three samples, the mean values of the scattering vector $\boldsymbol{q}_{mean}$ extracted from the Bragg reflection maps and strain ε_{mean}, calculated form $\boldsymbol{q}_{mean}$, are presented. Furthermore, the minimum q_{min} and maximum q_{max} value from a 10% threshold to the maximum intensity of the Bragg reflection maps are listed. The bending radius for R1 and R2 is calculated from q_{min} and q_{max}.

Sample	Contact metal	Φ_{bh} [eV]	n	q_{mean} [Å^{-1}]	ε_{mean} [10^{-3}]	q_{min} [Å^{-1}]	q_{max} [Å^{-1}]	Bending radius [mm]
R1	Ag	0.60 ± 0.02	5.4 ± 0.7	4.8246 ± 0.0008	0.63 ± 0.16	4.823 ± 0.0003	4.8266 ± 0.0003	74.5 ± 9.5
R2	Ag	0.70 ± 0.04	2.2 ± 0.4	4.8237 ± 0.0028	0.82 ± 0.55	4.8178 ± 0.0003	4.8293 ± 0.0003	6.4 ± 0.5
R3	Au	0.62 ± 0.01	5.9 ± 0.2	2.4436 ± 0.002	-12.19 ± 0.80	2.4392 ± 0.0002	2.4475 ± 0.0002	–

ZnO.[38] This may be due to crystalline defects in the ZnO as previous studies on Schottky contacts shown that the contact properties are immensely inflicted by defects near the interface[21,39] and that contact properties can be tailored by these.[22]

2.2. Scanning Nano XRD on ZnO Rods

Complementary scanning nano XRD was performed to investigate the crystalline structure in the three rods. The {0004} Bragg reflection was investigated for rod R1, R2, and the {0002} for R3. The respective rocking scans are shown in Figure 2d–f and were performed by varying the angle θ, see Figure 1a, with the X-ray beam positioned at the center of the rods at $x = 0$. These rocking scans were fitted with a Gaussian function, and a full width at half maximum (FWHM) of $0.027 \pm 0.003°$, $0.030 \pm 0.003°$, and $0.042 \pm 0.004°$ were found for R1, R2, and R3, respectively. From the Scherrer equation, the respective size of coherent scattering crystal volume was calculated to be 264.5 ± 45.6 nm, 236.3 ± 27.1 nm, and 317.5 ± 42.3 nm.[40] This is comparable to the volume probed by the X-ray nanobeam (beam size ($h \times v$) R1, R2: 250 nm × 350 nm; R3: 300 nm × 350 nm) and thus provides a lower limit for the size of coherent scattering regions in the crystal. After the rocking scans were measured, Bragg reflection maps were collected to further investigate the behavior of the three rods by performing line scans along the x axis. Figure 2g–i show Bragg reflection maps with fundamentally different behavior for the rods R1 to R3. Insets show cuts through the respective Bragg reflection map. For comparison, all three presented line scans were measured in the Ag (R1 and R2) or Au (R3) covered parts of the ZnO rod and are representative for the overall behavior of the respective sample, further scans from five different positions on the samples are shown in Figure S2–S4, Supporting Information. The values for the mean scattering vector $\boldsymbol{q}_{mean}$ and mean strain ε_{mean} in the rods and the minimum and maximum values q_{min} and q_{max} of the Bragg reflection maps are listed in Table 1. The q_{min} and q_{max} values are calculated as the minimum and maximum values of the scattering vector present in the Bragg reflection maps that show an intensity above a threshold of 10% of the maximum Bragg intensity. The Bragg reflection map of R1 in Figure 2g shows a well-defined distribution at each x position of the rod. In addition, a uniform, almost linear change from left to right is observed. The positive, tensile strain ε_{mean} in Table 1 indicates that the lattice constant of the rod is extended along the c axis and the linear change refers to a rod bending,[41] the left edge of the rod is compressed relative to an extended crystal size at the right edge. Therefore, the rod is bent toward the left with a bending radius of 74.5 mm. (For further information on the bending radius calculation see the Supporting Information.) Furthermore, toward the right edge, between the positions $x = -3$ µm and -18 µm, the distribution is split with the maximum intensity decreasing by an order of magnitude, the overall q distribution width increases and two local maximums emerge as shown in the inset of Figure 2g, more detailed in Figure S5, Supporting Information.

The Bragg reflection map of R2 shown in Figure 2h displays a hexagonal shape. In contrast to the behavior in sample R1 with its linear change, here, it shows a wide range of well-distributed crystal lattice sizes for all positions x. The huge FWHM of the Bragg reflection of 7.09×10^{-3} Å^{-1} in R2 exemplary at $x = 5$ µm compared to 6.7×10^{-4} Å^{-1} for R1 at position $x = 12$ µm can be considered an indication for smaller size of coherent scattering crystal volumes, microstrain in these volumes, or a combination of both. But, this is unlikely because the Bragg reflection map of R2 shows an almost homogeneous Bragg intensity distribution and no distinct maximum in most of the Bragg reflection map, as shown in the inset of Figure 2h and for further Bragg reflections see Figure S6, Supporting Information. It is more likely that this broadening is caused by a (macro)strain change along the probed crystal volume in the beam path (see Figure S8, Supporting Information) and is probably the result of a rod bending in z direction with a calculated radius of 6.4 mm. The bending, observed in R1 and R2, is likely the result of a mechanical stress induced while fixing the rod tips to two separate contacts of the sample holder to enable the electrical measurements.

The Bragg reflection map of R3 in Figure 2i displays a nonuniform behavior with a much higher absolute strain compared to the previous two rods. Moreover, peak splitting is observed multiple times across the rod with vastly varying q values and spatial sizes along the x direction. The peak splitting is shown in inset of Figure 2i and in Figure S7, Supporting Information. The peak splitting in the maps of R1 and prominently in R3 is a strong evidence for the presence of different, coexisting coherent scattering regions that exhibit small differences in lattice spacing and/or orientation. These can be caused by a plastic deformation and/or fracture of the crystal due to high stress along the c axis, even though a study showed that ZnO rods can be elastically strained beyond 3%.[42] This is well above the here reported strain. Furthermore, the effect is present in both tensile (R1) as well as compressive strained samples (R3) and opposing strains causing the same kind of crystal deformation is unlikely. A better explanation is the growth of a nonsingle crystalline ZnO structure in parts of R1 and in the majority of rod R3.

Examinations of the crystalline quality using TEM in combination with selected-area electron diffraction (ED) (SAED) were performed on a similar ZnO rod, grown by the flame transport

 © 2021 The Authors. Advanced Engineering Materials published by Wiley-VCH GmbH

synthesis. The micrometer dimensions of the ZnO rod limited the examined area to its tapered tip as shown in Figure S9, Supporting Information. ED pattern of a tilting series demonstrates that the ZnO rod exhibits a high crystal quality along the c axis showing strong diffraction patterns usually observed for a single component. However, ED patterns slightly tilted away from edge-on zone-axis observation conditions revealed multiple weak reflections which can indicate the presence of minor crystalline components[43] or can result from dynamical diffraction events in a thick specimen. See Figure S9, Supporting Information.

The growth of multiple crystals within the rod can lead to at least two possible impacts, first, a divergence of the lattice orientation and, second, different lattice parameters for the multiple (possibly strained) crystalline structures. In R3, it is likely that a combination of both effects is present, resulting in multiple crystallites with different lattice parameter and orientation. At domain boundaries, an increased density of crystal defects is expected, which is well known to influence the electrical properties of Schottky contacts.[21,22] This gives rise to the explanation that the earlier reported IV curves and the related electrical properties are the result of crystalline defects in the ZnO rods that got indirectly visualized by measuring multiple lattice parameter for different crystallites with nXRD. Furthermore, it appears that the number of different crystallites has an impact on the electrical properties, as well. In contrast to R1, microrod R3 with its apparent high amount of vastly differing crystallites exhibits a higher reverse current, possibly due to the higher number of domain boundaries and, therefore, defects that contribute to the generation recombination process in the Schottky depletion region and decrease in the barrier height, e.g., due to inhomogeneities.[7,38,39]

2.3. Strain Model for Hexagonal Structure

For a more quantitative description of the measured strain distributions, an analytical model was developed to simulate the strain in a hexagonal rod, see **Figure 3**. The model in the x/z plane is extended along the y direction. The volume of the simulated rod with diameter $d = 1$ µm is divided into 10 nm voxels and to each of the voxels a strain value from an idealized strain distribution is attributed. This strain ε includes a constant strain $\varepsilon_{\text{const}}$, from a mechanical stress along the rod, and a linear component ε_{lin}, accounting for a rod bending. The equation for the model strain ε is

$$\varepsilon(x_{\text{m}}, z_{\text{m}}) = \varepsilon_{\text{const}} + \varepsilon_{\text{lin}} \cdot \frac{x_{\text{m}}}{\frac{d}{2}} \tag{1}$$

Here, x_{m} and z_{m} are the model's spatial coordinates with the rod center at (0,0). These are comparable to the axes x and z in the measured data. A constant strain $\varepsilon_{\text{const}}$ is present within the whole volume, with an additional linear change ε_{lin} along the x_{m} direction. The rod diameter d is included to ensure that the maximum strain ε_{lin} is reached at the edges of the rod along the x axis. For the calculation of a model strain map, we recall that the X-ray beam probes at each x position a full cross section along y

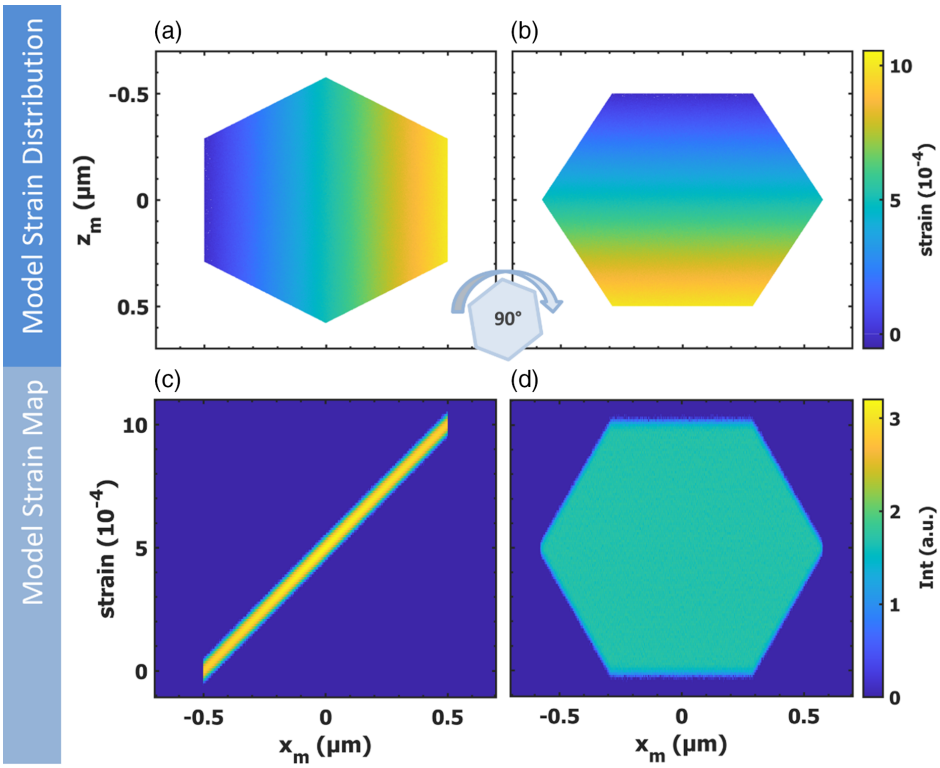

Figure 3. a) Strain distribution of a hexagonal-shaped model structure with a linear strain increase from left to right. b) The model is rotated clockwise by 90°. c,d) The respective strain maps calculated from the model strain distributions in the upper row, and the different orientation of the shape and strain directly influences the strain maps appearances.

© 2021 The Authors. Advanced Engineering Materials published by Wiley-VCH GmbH

15272648, 2021, 11, Downloaded from https://advanced.onlinelibrary.wiley.com/doi/10.1002/adem.202100201 by Christian-Albrechts-Universitat Zu Kiel, Wiley Online Library on [17/02/2026]. See the Terms and Conditions (https://onlinelibrary.wiley.com/terms-and-conditions) on Wiley Online Library for rules of use; OA articles are governed by the applicable Creative Commons License

15272648, 2021, 11, Downloaded from https://advanced.onlinelibrary.wiley.com/doi/10.1002/adem.202100201 by Christian-Albrechts-Universitat Zu Kiel, Wiley Online Library on [17/02/2026]. See the Terms and Conditions (https://onlinelibrary.wiley.com/terms-and-conditions) on Wiley Online Library for rules of use; OA articles are governed by the applicable Creative Commons License

through the sample. Assuming that scattering contributions from spatially separated crystallites adds up fully incoherent, the X-ray intensity distribution at a given strain value ε (or, more precisely, in an interval $\pm\Delta\varepsilon/2$ around this value) and position x is proportional to the sum of the intensities from all crystallites exhibiting this strain, along the beam path in y. The strain map visualizes the intensity for all strain values ε and all positions x across the sample. Replacing the X-ray intensity from crystallites in the real measurement with an amount of model voxels, exhibiting a strain in the specific range $\pm\Delta\varepsilon/2$, and the result is an artificial map $I(x_m,\varepsilon)$ of the simulated strain in the rod.

Figure 3a shows the strain distribution inside a model rod with a constant offset $\varepsilon_{const} = 0.5 \times 10^{-3}$ and a linear contribution $\varepsilon_{lin} = 0.5 \times 10^{-3}$. In this way, the strain change from the left to the right edge of the rod is 0 to 1×10^{-3}. For Figure 3b, the same model strain distribution is rotated clockwise around the y axis by 90°. From these simulated strain distributions, the respective strain maps were calculated, as described earlier. In Figure 3c, the strain map of the first artificial strain distribution is displayed. It shows a linear strain change left to right from 0 to 1×10^{-3} and a mean strain of 0.5×10^{-3}, as expected. The second strain map in Figure 3d, calculated from the rotated strain distribution, has a mean strain of 0.5×10^{-3}, as well. But, it shows no linear increase in the strain in any direction, instead a well-distributed broadening of the strain ranging from 0 to 1×10^{-3} with a reduced strain intensity.

These simulations imply that the Bragg reflection maps in Figure 2d–f, displaying a striking similarity to the strain maps in Figure 3c,d, are linked to the strain distribution and further, that the q range and shape of the maps are a direct result of the present strain distribution in the rods. Furthermore, the Bragg reflection maps in Figure 2d,e for R1 and R2 are comparable, but are mainly different due to a rotated strain-to-probing orientation, likely due to bending in two perpendicular directions. This explains the qualitatively comparable *IV* curves despite the difference in the respective strain maps.

In this article, a Schottky barrier height change of around 14% is reported, linked to the crystal quality. This change is by one order of magnitude stronger than a piezotronic induced height change of a Ag/ZnO Schottky barrier due to an applied mechanical stress of 70 MPa.[44] Another study reported a temperature-dependent Schottky barrier height change in 35% for a temperature drop from 300 to 77 K and attributed this change to a lowering of the carrier density with decreasing temperature.[45] The carrier density can also be altered by doping the ZnO, e.g., with boron atoms.[46] For graphene/ZnO contacts, the Schottky barrier height was found to first increase with rising boron doping concentration but to decrease below the intrinsic height after reaching a doping level of 0.15 mol l^{-1}, with a relative Schottky barrier height change in 56%.[46] In summary, the impact of the crystal quality is bigger than the strain-induced change by the piezotronic effect, but is smaller than that of temperature or doping concentration induced changes. Furthermore, the reported impact of the crystalline quality is not solely limited to an altering Schottky barrier height but, as well, causes a change of the *IV* characteristics ranging from rectifying Schottky diode to ohmic behavior, as it is known for different contact materials.[18] Therefore, the impact of ZnO crystalline quality is diverse and should be considered when designing devices and sensors.

3. Conclusions

In conclusion, following the electric characterization of Schottky contacts using *IV* curves, the crystal structure in three ZnO microrods was spatially resolved measured by nXRD. It was found that a well-defined strain distribution, with nonabrupt changes in the measured crystal lattice parameter, is strongly linked to the rectifying Schottky diode characteristics. In contrast, a highly strained crystal, exhibiting several coherent scattering domains rather than a single domain, causes nonideal *IV* characteristics, probably due to increased defect rates at the domain boundaries. It is shown that the crystallinity in semiconductor material has an immense impact on their electrical properties and strain revealing nXRD holds an opportunity to characterize the crystalline structure in semiconductor-based devices and enhance their performance. Further investigations of the crystallinity and a better understanding of its impact on the performance of piezotronic devices are a key for the optimization of such sensors. To this end, advanced techniques to investigate the crystalline structure are extremely helpful. A combined approach using highly resolved TEM measurements,[47] multi Bragg diffraction,[48] and visualizations of the 3D strain distributions by coherent X-ray diffraction imaging[49,50] or ptychography[51,52] can provide deeper insights in the future studies. For textured or polycrystalline samples, texture investigations,[53] or extending investigations to amorphous systems, pair distribution function analysis from total scattering would be beneficial.[54,55] It is clear that X-ray techniques in particular, when combined with TEM, can deliver useful information for enhancing device design and performance.

4. Experimental Section

Sample Preparation: Flame transport synthesis was used for the production of the ZnO microstructures.[56] With this technique, it was possible to produce tailor-made ZnO rods with diameters ranging from below 1 µm to a few hundred µm and lengths up to mm. Three ZnO rods were used, R1 to R3. The diameters of the samples were 55.5 ± 0.6 µm, 15.2 ± 0.6 µm, and 51.3 ± 0.6 µm, respectively. These were determined from optical images, see Figure S10, Supporting Information. After both rod tips were fixed with epoxy to a sample holder, one end of the rod was coated with 100 nm Al to create an ohmic contact, the other end was covered in Ag glue, for sample R3, this end was first coated with 200 nm of gold by thermal evaporation and then partly covered with Ag glue. The Ag and Au on the ZnO established a Schottky contact. Furthermore, the Ag glue was used at all contacts to fix and connect wires for the electrical measurements. An uncoated part in the middle of the ZnO rod was left free to prevent a short circuit between the Ag or Au contact and the Al.

Scanning nXRD: The experiment was performed at the Nanofocus endstation of the beamline P03 at the Petra III synchrotron at DESY.[57,58] The photon energy was 13 keV and the beam was focused with a Kirkpatrick–Baez mirror[59] down to 250×350 nm^2 ($h \times v$) at the sample position. The first step was the initial search for the Bragg reflection by using a Pilatus 300 k (R1 and R2) and Pilatus 1M (R3) with a sample detector distance of 24 cm to increase the observed q space. In a time-consuming procedure, it was necessary to search for, find, and optimize the individual reflections of the {0004} (R1 R2), and {0002} (sample R3)

© 2021 The Authors. Advanced Engineering Materials published by Wiley-VCH GmbH

Bragg reflections. To illustrate the high crystallinity of the rods, rocking scans were collected and the summed up detector images of these scans shown in Figure S10, Supporting Information illustrating a narrow, high intense distribution of the selected Bragg peak. Further reflections found for R1 and prominently R3 were identified as Bragg reflections of the silver and gold coating, respectively. Further data were acquired using a Photonic Science CCD camera with 65 µm square-sized pixels at a detector sample distance of 1.58 m for samples R1 and R2, and 2.56 m for R3. First, a rocking scan was conducted to optimizing the scattered intensity by rotating the rods around the *x* axis (Figure 1a) and, second, a line scan in *x* direction across the whole ZnO rod with 200 nm spatial step width. For the calculation of the coherent scattering crystal volume size w_{DS}, the Scherrer equation was used, $w_{DS} = \frac{K\lambda}{\Delta(2\theta_0)\theta_0}$, with $K = 0.89$, X-ray wavelength λ, FWHM of the Bragg reflection $\Delta(2\theta_0)$ in radians, and the Bragg angle θ_0.[40] FWHM and peak width parameter sigma σ of a Gaussian function are related by, $FWHM = 2\sqrt{2\ln 2}\sigma$.

Current/Voltage Measurements: The combination of a Schottky and an ohmic contact allowed one to measure the forward and reverse current of the Schottky contact. For the electrical measurements, a Keithley 2450 Sourcemeter was used to collect the *IV* curves in a range of −2 to 2 V with a resolution of 0.1 V for the samples R1 and R2, and −1 to 1 V with 0.02 V steps for sample R3. The current accuracy was between 1×10^{-9} and 6×10^{-11} A and further 7×10^{-4} V for the sourced voltage. To distinguish the barrier height and ideality factor of the Schottky contact, a linear function was fitted to the logarithm of the current in the range of 0.1 to 0.3 V.[38] The intersection of the fitted line with the *y* axis defined the current I_0 and further the barrier height $\phi_{bh} = \frac{kT}{q}\ln\left(\frac{A^* T^2}{J_0}\right)$,[38] with the Boltzmann constant *k*, temperature $T = 294$ K, elementary charge *q*, effective Richardson constant $A^* = 32$ A cm^{-2} K^{-2},[60,61] and the current density J_0 equals the current I_0 divided by the contact area size. From the fitted slope $\frac{d(\ln J)}{dV}$ of the fitted linear function, the ideality factor *n* is distinguished by employing $n = \frac{q}{kT}\frac{dV}{d(\ln J)}$.[38]

Transmission Electron Microscopy: TEM had been performed to study the crystallinity of the ZnO microstructures. The ZnO samples were transferred to TEM Cu-lacey grids with carbon support film after gentle crushing and dispersing them in butanol. A SAED tilting series on a ZnO microneedle was performed on a JEOL JEM2100 (LaB_6, 200 kV) microscope.

Supporting Information

Supporting Information is available from the Wiley Online Library or from the author.

Acknowledgements

Funded by the German Research Foundation (DFG, Deutsche Forschungsgemeinschaft) through the Collaborative Research Centre CRC 1261 "Magnetoelectric Sensors: From Composite Materials to Biomagnetic Diagnostics" via project A6. The authors acknowledge DESY (Hamburg, Germany), a member of the Helmholtz Association HGF, for the provision of experimental facilities. Parts of this research were conducted at PETRA III and the authors would like to thank the staff of beamline P03/MiNAXS for the support during the experiments. Furthermore, the authors would like to thank M. Greve for the help in designing the sample holder, the workshop of the physics department/Kiel University for the construction of the sample environment and Dennis Kiel, Keyence Deutschland GmbH, for collecting the optical digital microscope pictures.

Open access funding enabled and organized by Projekt DEAL.

Conflict of Interest

The authors declare no conflict of interest.

Data Availability Statement

The data that support the findings of this study are available from the corresponding author upon reasonable request.

Keywords

current–voltage curves, nano X-ray diffractions, Schottky contact, strain, ZnO

Received: February 15, 2021
Revised: April 8, 2021
Published online: May 2, 2021

[1] J. Ma, J. Hu, Z. Li, C.-W. Nan, *Adv. Mater.* **2011**, *23*, 1062.
[2] N. A. Spaldin, R. Ramesh, *Nat. Mater.* **2019**, *18*, 203.
[3] E. Lage, C. Kirchhof, V. Hrkac, L. Kienle, R. Jahns, R. Knöchel, E. Quandt, D. Meyners, *Nat. Mater.* **2012**, *11*, 523.
[4] P. Hayes, S. Salzer, J. Reermann, E. Yarar, V. Röbisch, A. Piorra, D. Meyners, M. Höft, R. Knöchel, G. Schmidt, E. Quandt, *Appl. Phys. Lett.* **2016**, *108*, 182902.
[5] H. Greve, E. Woltermann, H. J. Quenzer, B. Wagner, E. Quandt, *Appl. Phys. Lett.* **2010**, *96*, 7.
[6] R. T. Tung, *Phys. Rev. Lett.* **1984**, *52*, 461.
[7] R. T. Tung, *Appl. Phys. Rev.* **2014**, *1*, 11304.
[8] Z. L. Wang, *Adv. Mater.* **2007**, *19*, 889.
[9] L. Wang, Z. L. Wang, *Nano Today* **2021**, *37*, 101108.
[10] J. Zhou, Y. Gu, P. Fei, W. Mai, Y. Gao, R. Yang, G. Bao, Z. L. Wang, *Nano Lett.* **2008**, *8*, 3035.
[11] G. Hu, Y. Zhang, L. Li, Z. L. Wang, *ACS Nano* **2018**, *12*, 779.
[12] J. Zhu, X. Zhou, L. Jing, Q. Hua, W. Hu, Z. L. Wang, *ACS Nano* **2019**, *13*, 13161.
[13] Y. S. Zhou, K. Wang, W. Han, S. C. Rai, Y. Zhang, Y. Ding, C. Pan, F. Zhang, W. Zhou, Z. L. Wang, *ACS Nano* **2012**, *6*, 6478.
[14] M. Mintken, M. Schweichel, S. Schröder, S. Kaps, J. Carstensen, Y. K. Mishra, T. Strunskus, F. Faupel, R. Adelung, *Nano Energy* **2019**, *56*, 420.
[15] Y. Chen, G. Gao, J. Zhao, H. Zhang, J. Yu, X. Yang, Q. Zhang, W. Zhang, S. Xu, J. Sun, Y. Meng, Q. Sun, *Adv. Funct. Mater.* **2019**, *29*, 1900959.
[16] Z. L. Wang, J. Song, *Science (80-.).* **2006**, *312*, 242.
[17] S. Yang, L. Wang, X. Tian, Z. Xu, W. Wang, X. Bai, E. Wang, *Adv. Mater.* **2012**, *24*, 4676.
[18] L. J. Brillson, Y. Lu, *J. Appl. Phys.* **2011**, *109*, 121301.
[19] W. Walukiewicz, *Phys. Rev. B* **1988**, *37*, 4760.
[20] M. W. Allen, S. M. Durbin, *Appl. Phys. Lett.* **2008**, *92*, 122110.
[21] L. J. Brillson, H. L. Mosbacker, M. J. Hetzer, Y. Strzhemechny, G. H. Jessen, D. C. Look, G. Cantwell, J. Zhang, J. J. Song, *Appl. Phys. Lett.* **2007**, *90*, 102116.
[22] J. W. Cox, M. Foster, A. Jarjour, H. Von Wenckstern, M. Grundmann, L. J. Brillson, *Nano Lett.* **2018**, *18*, 6974.
[23] R. C. Rogan, N. Tamura, G. A. Swift, E. Üstündag, *Nat. Mater.* **2003**, *2*, 379.
[24] T. U. Schulli, S. J. Leake, *Curr. Opin. Solid State Mater. Sci.* **2018**, *22*, 188.
[25] J. Todt, C. Krywka, Z. L. Zhang, P. H. Mayrhofer, J. Keckes, M. Bartosik, *Acta Mater.* **2020**, *195*, 425.
[26] J. Keckes, M. Bartosik, R. Daniel, C. Mitterer, G. Maier, W. Ecker, J. Vila-Comamala, C. David, S. Schoeder, M. Burghammer, *Scr. Mater.* **2012**, *67*, 748.

© 2021 The Authors. Advanced Engineering Materials published by Wiley-VCH GmbH

15272648, 2021, 11, Downloaded from https://advanced.onlinelibrary.wiley.com/doi/10.1002/adem.202100201 by Christian-Albrechts-Universitat Zu Kiel, Wiley Online Library on [17/02/2026]. See the Terms and Conditions (https://onlinelibrary.wiley.com/terms-and-conditions) on Wiley Online Library for rules of use; OA articles are governed by the applicable Creative Commons License

[27] M. Barchuk, M. Motylenko, T. Schneider, M. Förste, C. Röder, A. Davydok, S. Lazarev, C. Schimpf, C. Wüstefeld, O. Pätzold, D. Rafaja, *J. Appl. Phys.* **2019**, *126*, 085301.
[28] S. B. Hrkac, M. Abes, C. T. Koops, C. Krywka, M. Müller, S. Kaps, R. Adelung, J. McCord, E. Lage, E. Quandt, O. M. Magnussen, B. M. Murphy, *Appl. Phys. Lett.* **2013**, *103*, 1.
[29] S. B. Hrkac, C. T. Koops, M. Abes, C. Krywka, M. Müller, M. Burghammer, M. Sztucki, T. Dane, S. Kaps, Y. K. Mishra, R. Adelung, J. Schmalz, M. Gerken, E. Lage, C. Kirchhof, E. Quandt, O. M. Magnussen, B. M. Murphy, *ACS Appl. Mater. Interfaces* **2017**, *9*, 25571.
[30] C. M. Lueng, H. L. W. Chan, C. Surya, C. L. Choy, *J. Appl. Phys.* **2000**, *88*, 5360.
[31] M. Catti, Y. Noel, R. Dovesi, *J. Phys. Chem. Solids* **2003**, *64*, 2183.
[32] S. Desgreniers, *Phys. Rev. B: Condens. Matter Mater. Phys.* **1998**, *58*, 14102.
[33] B. H. Erich Kisi, M. M. Elcombe, *Acta Cryst.* **1989**, *C45*, 1867.
[34] L. Gerward, J. S. Olsen, *J. Synchrotron Rad.* **1995**, *2*, 233.
[35] R. R. Reeber, *J. Appl. Phys.* **1970**, *41*, 5063.
[36] M. Abes, C. T. Koops, S. B. Hrkac, E. Quandt, L. Bouchenoire, B. M. Murphy, O. M. Magnussen, *J. Appl. Phys.* **2013**, *113*, 124303.
[37] Y. Zhao, J. Zhang, *J. Appl. Crystallogr.* **2008**, *41*, 1095.
[38] S. M. Sze, K. K. Ng, *Physics of Semiconductor Devices*, Wiley-Interscience **2006**, ISBN: 978-0-471-14323-9.
[39] Y. Li, Y. Li, J. Zhang, *Mater. Sci. Semicond. Process.* **2020**, *106*, 104793.
[40] J. I. Langford, A. J. C. Wilson, *J. Appl. Crystallogr.* **1978**, *11*, 102.
[41] W. A. Adeagbo, S. Thomas, S. K. Nayak, A. Ernst, W. Hergert, *Phys. Rev. B: Condens. Matter Mater. Phys.* **2014**, *89*, 195135.
[42] R. Agrawal, B. Peng, E. E. Gdoutos, H. D. Espinosa, *Nano Lett.* **2008**, *8*, 3668.
[43] N. Wolff, V. Hrkac, J. J. Ditto, V. Duppel, Y. K. Mishra, D. C. Johnson, R. Adelungd, L. Kienle, *J. Appl. Crystallogr.* **2019**, *52*, 1009.
[44] P. Keil, T. Frömling, A. Klein, J. Rödel, N. Novak, *J. Appl. Phys.* **2017**, *121*, 155701.
[45] Y. Hu, B. D. B. Klein, Y. Su, S. Niu, Y. Liu, Z. L. Wang, *Nano Lett.* **2013**, *13*, 5026.
[46] Y. Li, Y. Li, J. Zhang, T. Tong, W. Ye, *J. Phys. D. Appl. Phys.* **2018**, *51*, 095104.
[47] C. Zhang, K. L. Firestein, J. F. S. Fernando, D. Siriwardena, J. E. Treifeldt, D. Golberg, *Adv. Mater.* **2020**, *32*, 1904094.
[48] A. Johannes, J. Rensberg, T. A. Grünewald, P. Schöppe, M. Ritzer, M. Rosenthal, C. Ronning, M. Burghammer, *J. Appl. Crystallogr.* **2020**, *53*, 99.
[49] X. Shi, N. Burdet, B. Chen, G. Xiong, R. Streubel, R. Harder, I. K. Robinson, *Appl. Phys. Rev.* **2019**, *6*, 11306.
[50] J. Carnis, L. Gao, S. Labat, Y. Y. Kim, J. P. Hofmann, S. J. Leake, T. U. Schülli, E. J. M. Hensen, O. Thomas, M. I. Richard, *Sci. Rep.* **2019**, *9*, 1.
[51] M. Holler, M. Guizar-Sicairos, E. H. R. Tsai, R. Dinapoli, E. Müller, O. Bunk, J. Raabe, G. Aeppli, *Nature* **2017**, *543*, 402.
[52] F. Pfeiffer, *Nat. Photonics* **2018**, *12*, 9.
[53] K. M. Howell, W. Bashir, A. De Pastina, R. Matloub, P. Muralt, L. G. Villanueva, *J. Vas. Sci. Technol.* **2018**, *37*, 021504.
[54] F. X. Zhang, S. Zhao, K. Jin, H. Xue, G. Velisa, H. Bei, R. Huang, J. Y. P. Ko, D. C. Pagan, J. C. Neuefeind, W. J. Weber, Y. Zhang, *Phys. Rev. Lett.* **2017**, *118*, 205501.
[55] M. Roelsgaard, A. C. Dippel, K. A. Borup, I. G. Nielsen, N. L. N. Broge, J. T. Röh, O. Gutowski, B. B. Iversen, *IUCrJ* **2019**, *6*, 299.
[56] Y. K. Mishra, S. Kaps, A. Schuchardt, I. Paulowicz, X. Jin, D. Gedamu, S. Freitag, M. Claus, S. Wille, A. Kovalev, S. N. Gorb, R. Adelung, *Part. Part. Syst. Charact.* **2013**, *30*, 775.
[57] A. Buffet, A. Rothkirch, R. Döhrmann, V. Körstgens, M. M. Abul Kashem, J. Perlich, G. Herzog, M. Schwartzkopf, R. Gehrke, P. Müller-Buschbaum, S. V. Roth, *J. Synchrotron Radiat.* **2012**, *19*, 647.
[58] C. Krywka, H. Neubauer, M. Priebe, T. Salditt, J. Keckes, A. Buffet, S. V. Roth, R. Doehrmann, M. Mueller, *J. Appl. Crystallogr.* **2012**, *45*, 85.
[59] C. Krywka, M. Müller, in *X-Ray Diffraction Modelling and Experimental Techniques*, Pan Stanford Publishing Pte. Ltd., **2015**, pp. 55–88, ISBN: 9789814303590.
[60] J.-J. Wu, D. K.-P. Wong, *Adv. Mater.* **2007**, *19*, 2015.
[61] L. Schmidt-Mende, J. L. MacManus-Driscoll, *Mater. Today* **2007**, *10*, 40.

© 2021 The Authors. Advanced Engineering Materials published by Wiley-VCH GmbH

15272648, 2021, 11, Downloaded from https://advanced.onlinelibrary.wiley.com/doi/10.1002/adem.202100201 by Christian-Albrechts-Universitat Zu Kiel, Wiley Online Library on [17/02/2026]. See the Terms and Conditions (https://onlinelibrary.wiley.com/terms-and-conditions) on Wiley Online Library for rules of use; OA articles are governed by the applicable Creative Commons License